ChemComm

COMMUNICATION

View Article Online
View Journal | View Issue

Published on 20 August 2014. Downloaded by Universiteit van Amsterdam on 17/09/2014 07:49:39.

Cite this: *Chem. Commun.*, 2014, **50**, 12105

Received 28th July 2014,
Accepted 20th August 2014

DOI: 10.1039/c4cc05833j

www.rsc.org/chemcomm

Enhanced CO_2 sorption and selectivity by functionalization of a NbO-type metal–organic framework with polarized benzothiadiazole moieties†

Chengling Song,[a] Yabing He,*[a] Bin Li,[b] Yajing Ling,[a] Hailong Wang,[b] Yunlong Feng,[a] Rajamani Krishna[c] and Banglin Chen*[b]

A new NbO-type metal–organic framework ZJNU-40 incorporating highly polarized benzothiadiazole moieties exhibits a high CO_2 uptake of 108 cm^3 g^{-1} at 296 K and 1 atm, as well as good adsorption selectivities of CO_2 over CH_4 and N_2 at room temperature, which is superior to that of the analogous MOF NOTT-101.

The escalating level of atmospheric CO_2 is a subject of widespread public concern associated with global warming and climate change, and consequently, there remains an urgent need to selectively capture and sequester CO_2 to reduce its greenhouse effect in the atmosphere. Most of the CO_2 capture processes make use of liquid amine-based absorbents to chemically adsorb CO_2; however, they suffer from the drawbacks of the corrosive nature of the solvents and high energy demand for solvent regeneration. In contrast, using porous materials to capture CO_2 appears to be an energy-efficient alternative approach due to their low energy requirements, thus stimulating extensive efforts to find suitable adsorbents for removing CO_2. In this regard, metal–organic frameworks (MOFs), an emerging class of porous materials, have shown charming properties with respect to CO_2 storage and separation because their chemically adjustable organic and inorganic moieties can be carefully predesigned to direct the molecular recognition of CO_2.[1] In fact, several MOFs with large CO_2 storage capacity and high selectivity have been recently reported.[2]

Of various porous MOFs, the NbO-type **MOF-505** series constructed from dicopper paddlewheels and diisophthalates has attracted tremendous attention because this class of MOF materials exhibit excellent gas sorption properties due to their high surface area, tunable pore size and open copper sites suitable for gas adsorption. Some of them exhibited high adsorption capacity for H_2 and CH_4.[3] To improve the ability of NbO-type MOFs for CO_2 capture and separation, great efforts have been devoted to tune the pore size/shape and/or engineer surface chemistry. It has been reported that the inclusion of some active binding sites into the framework such as NO_2, amide, imide, and oxalamide is capable of increasing CO_2 binding affinity.[4] Since benzothiadiazole containing two nitrogen and one sulfur atoms is a polar, fused heterocyclic building block with the molecular dipole of 4.8 Debye estimated by Chemical 3D software, we plan to incorporate such a highly polarized benzothiadiazole unit as a spacer between two isophthalate moieties to develop a new tetracarboxylic acid (H_4L, Scheme 1), and with which to target the corresponding NbO-type MOF designated as **ZJNU-40**. With a moderate surface area of 2209 m^2 g^{-1}, open metal sites (OMSs) of 1.52 nm^{-3}, accessible donor sites, two types of nanoscopic cages, and a polarized cage surface within the framework, the activated **ZJNU-40a** exhibits high CO_2 *uptake capacity*, as well as good *adsorption selectivity* of CO_2 over CH_4 and N_2, which is superior to that of the analogous MOF **NOTT-101** constructed from 1,4-benzenediisophthalate ligands of the same length as H_4L.

The organic linker H_4L, 5,5′-benzo[*c*][1,2,5]thiadiazole-4,7-diyl-diisophthalic acid, was readily synthesized by a Suzuki cross-coupling of 4,7-dibromobenzo[*c*][1,2,5]thiadiazole and dimethyl (5-pinacolboryl)isophthalate followed by hydrolysis and acidification. **ZJNU-40** was obtained as blue rhombic crystals *via* a solvothermal reaction of the organic ligand and $Cu(NO_3)_2{\cdot}3H_2O$ in a mixed solvent of *N*,*N*-diethylformamide (DEF) and H_2O

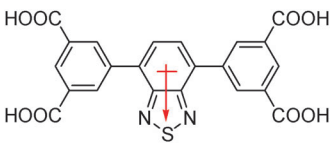

Scheme 1 The organic building block H_4L used to construct the MOF **ZJNU-40**, with the local molecular dipole moment, highlighted in red, perpendicular to the molecular long axis.

[a] *College of Chemistry and Life Sciences, Zhejiang Normal University, Jinhua 321004, China. E-mail: heyabing@zjnu.cn*
[b] *Department of Chemistry, University of Texas at San Antonio, One UTSA Circle, San Antonio, Texas 78249-0698, USA. E-mail: banglin.chen@utsa.edu*
[c] *Van't Hoff Institute for Molecular Sciences, University of Amsterdam Science Park 904, 1098 XH Amsterdam, The Netherlands*

† Electronic supplementary information (ESI) available: Synthesis and characterization, PXRD, TGA, sorption isotherms, IAST and breakthrough calculations. CCDC 1014276. For ESI and crystallographic data in CIF or other electronic format see DOI: 10.1039/c4cc05833j

Published on 20 August 2014. Downloaded by Universiteit van Amsterdam on 17/09/2014 07:49:39.

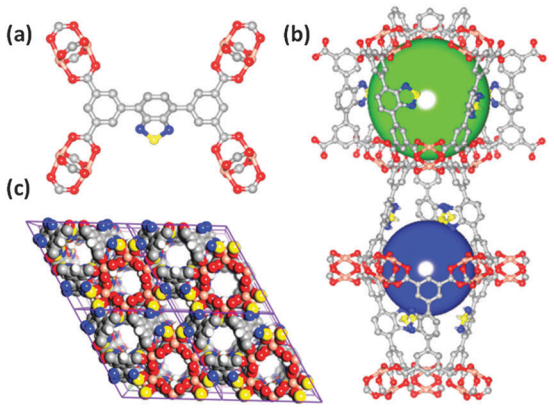

Fig. 1 Single-crystal X-ray structure of **ZJNU-40**. (a) Each organic linker connects with four dicopper paddlewheel $Cu_2(COO)_4$ units; (b) two types of nanocages; (c) CPK representation of a 3D open framework viewed along the *c* direction.

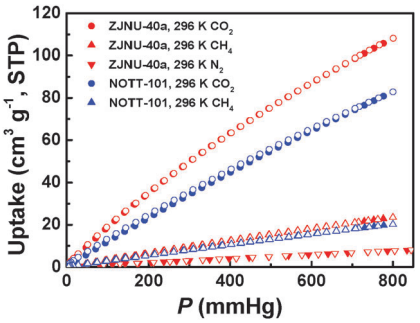

Fig. 2 CO_2, CH_4, and N_2 sorption isotherms of **ZJNU-40a** (red) and **NOTT-101** (blue) at 296 K. The solid and open symbols represent adsorption and desorption, respectively.

under acidic conditions. The crystal structure was characterized by single-crystal X-ray diffraction studies, and the phase purity of the bulk material was verified by powder X-ray diffraction (PXRD, Fig. S1, ESI†). Based on the single-crystal X- ray diffraction structure determination, thermogravimetric analysis (TGA, Fig. S2, ESI†) and microanalysis, **ZJNU-40** can be formulated as $[Cu_2L(H_2O)_2]\cdot 4DEF\cdot 6H_2O$.

Single-crystal X-ray diffraction analysis revealed that **ZJNU-40** is isoreticular to **NOTT-101**. As expected, a pair of copper centers are linked by four bridging carboxylates to form a paddlewheel secondary building unit (SBU) serving as a 4-connected square-planar node, which is bridged by the 4-connected rectangular organic building blocks to form a three-dimensional (3D) noninterpenetrated 4,4-connected NbO-type network (Fig. 1). Alternatively, if the bridging organic linker is considered as having two 3-coordinated (3-c) branch points, then in combination with the 4-coordinated dicopper paddlewheels, the derived net is the one with the RCSR symbol fof.[5] Interestingly, the central benzothiadiazole sites remain unbound, and thus provide additional gas binding sites. If the centers of dicopper paddlewheel SBUs are taken as vertices of polyhedra, the framework of **ZJNU-40** contains two distinct types of nanoscopic cages shown in Fig. 1b. The small octahedral cage consists of 12 ligands and 6 paddlewheel SBUs, and the diameter is about 12 Å, taking into account the van der Waals radii of the atoms; while the large cuboctahedral cage is constructed from 6 ligands and 12 paddlewheel SBUs with dimensions of *ca.* 9 × 18 Å. It is worth noting that the two cages are densely decorated with a big molecular dipole of benzothiadiazole functionalities.

The permanent porosity was unambiguously established by the N_2 sorption isotherm at 77 K. Prior to gas sorption analysis, the as-prepared **ZJNU-40** was solvent-exchanged with dry acetone and then evacuated at 373 K under dynamic vacuum, generating the activated **ZJNU-40a**. The integrity of the framework was confirmed by powder X-ray diffraction (Fig. S1, ESI†). The nitrogen sorption isotherms at 77 K reveal a typical reversible type-I sorption behavior (Fig. S3, ESI†), characteristic of microporous materials. Based on the N_2 sorption isotherms, Brunauer–Emmett–Teller (BET) and Langmuir surface areas were estimated to be 2209, and 2328 $m^2\ g^{-1}$, respectively (Fig. S4, ESI†). The pore volume calculated from the maximum amount of N_2 adsorbed is 0.88 $cm^3\ g^{-1}$. These values are lower than those of **NOTT-101**[3] due to the presence of the thiadiazole moieties pointing to the pore, but are comparable to those of some copper-based NbO-type frameworks such as **NOTT-105**,[3a] **NOTT-125a**,[4e] **PCN-16**,[6] **NU-135**,[7] **UTSA-80**,[8] **SNU-50**,[4c] **NJU-Bai14**[4a] and **HNUST-2**[9] (Table S2, ESI†).

Establishment of permanent porosity prompts us to examine its utility as an adsorbent for CO_2 capture and separation. Accordingly, CO_2, CH_4 and N_2 sorption isotherms were collected up to 1 atm at two different temperatures of 273 K and 296 K. As shown in Fig. 2, the isotherms are completely reversible and show no hysteresis. At 1 atm, **ZJNU-40a** exhibited a CO_2 uptake of 170 and 108 cm^3 (STP) g^{-1} at 273 and 296 K, respectively, corresponding to about 40 and 26 CO_2 molecules per unit cell. Remarkably, this gravimetric CO_2 adsorption capacity at room temperature is significantly higher than that of **NOTT-101** (83 $cm^3\ g^{-1}$), and is among the highest reported for isoreticular Cu-based NbO-type MOFs (Table S2, ESI†): **MOF-505**[2a] (73 $cm^3\ g^{-1}$), **NOTT-101** (83 $cm^3\ g^{-1}$), **NOTT-102** (72 $cm^3\ g^{-1}$), **UTSA-40**[10] (73 $cm^3\ g^{-1}$), **NU-135**[7] (79 $cm^3\ g^{-1}$), **SNU-50**[4c] (80 $cm^3\ g^{-1}$), **NOTT-125**[4e] (93 $cm^3\ g^{-1}$), **HNUST-1**[4b] (93 $cm^3\ g^{-1}$), **NJU-Bai14**[4a] (100 $cm^3\ g^{-1}$), and **Cu_2(dbip)**[11] (122 $cm^3\ g^{-1}$). In sharp contrast to CO_2, **ZJNU-40a** can adsorb only limited amounts of CH_4 and N_2, indicating that **ZJNU-40a** has potential application in the separation of CO_2–CH_4 and CO_2–N_2 mixtures.

Ideal Adsorbed Solution Theory (IAST) was used to calculate the adsorption selectivities and CO_2 uptake of **ZJNU-40** and **NOTT-101** for the following binary gas mixtures: 50/50 CO_2/CH_4, 5/95 CO_2/CH_4, and 15/85 CO_2/N_2. These mixtures mimic biogas treatment, natural gas upgrading, and post-combustion capture applications, respectively. Fig. S8 (ESI†) presents the values of the adsorption selectivity for these gas mixtures maintained under isothermal conditions at 296 K in **ZJNU-40a** and **NOTT-101**. It can be seen that **ZJNU-40a** has much higher selectivity towards CO_2 for all three mixture compositions. Fig. S9 (ESI†) presents IAST calculations for CO_2 uptake from 50/50 CO_2/CH_4, 5/95 CO_2/CH_4, and 15/85 CO_2/N_2 gas mixtures maintained under isothermal conditions at 296 K in **ZJNU-40a**, and **NOTT-101**.

 This journal is © The Royal Society of Chemistry 2014

Published on 20 August 2014. Downloaded by Universiteit van Amsterdam on 17/09/2014 07:49:39.

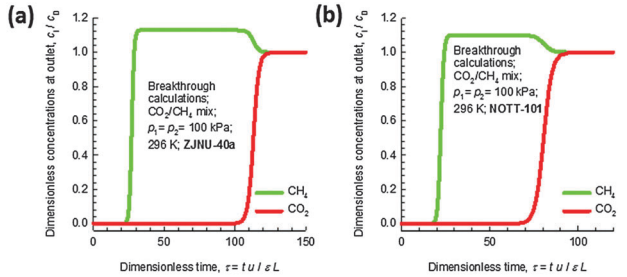

Fig. 3 50/50 CO_2/CH_4 mixture breakthrough characteristics as a function of the dimensionless time in an adsorber packed with (a) **ZJNU-40a**, and (b) **NOTT-101** and maintained under isothermal conditions at 296 K. In these calculations the total pressure is maintained at 200 kPa.

Again, **ZJNU-40a** has a much higher CO_2 uptake in all three cases. The combination of higher CO_2 uptake capacity and higher adsorption selectivity of CO_2 over CH_4 and N_2 will lead to a better separation performance of **ZJNU-40a**.

To further compare the separation performance of **ZJNU-40a** and **NOTT-101**, we perform transient breakthrough simulations using the methodology described in the literature.[12] The details are provided in ESI.† Fig. 3 compares 50/50 CO_2/CH_4 mixture breakthrough characteristics as a function of the dimensionless time in an adsorber packed with **ZJNU-40a** and **NOTT-101** and maintained at 296 K and a total pressure of 200 kPa. The breakthrough of CO_2 occurs at a later time with **ZJNU-40a**, indicating that this material has a better separation performance. Furthermore, based on the material balance on the fixed bed adsorber, the productivities of methane with a purity of 99.95%+ are calculated to be 2.84 mol per kg of **ZJNU-40a**, and 1.78 mol per kg of **NOTT-101** (Fig. S11 and 12, ESI†). This implies that **ZJNU-40a** has a 50% higher productivity than **NOTT-101**. Likewise, when separation of 5/95 CO_2/CH_4 mixtures at 296 K and a total pressure of 200 kPa is considered, the productivities of methane with a purity of 99.95%+ are calculated to be 5.80 mol per kg of **ZJNU-40a**, and 3.62 mol per kg of **NOTT-101** (Fig. S13 and 14, ESI†). These productivity values are higher than the corresponding ones for 50/50 CO_2/CH_4 mixtures because a lower amount of CO_2 needs to be captured. For 5/95 CO_2/CH_4 mixtures, **ZJNU-40a** has a 60% higher productivity than **NOTT-101**. As for the separation of 15/85 CO_2/N_2 gas mixtures at 296 K and a total pressure of 100 kPa, the productivities of N_2 with a purity of 99.95%+ can be determined to be 3.29 mol per kg of **ZJNU-40a**, and 2.08 mol per kg of **NOTT-101** (Fig. S15 and 16, ESI†). Taken together, these breakthrough calculations clearly demonstrate that **ZJNU-40a** has a better separation performance than **NOTT-101**.

To understand the gas-framework interaction, the coverage dependent adsorption enthalpies were calculated using the Clausius–Clapeyron equation by fitting the adsorption isotherms taken at 273 and 296 K to the Langmuir expression. As expected (Fig. S17, ESI†), **ZJNU-40a** exhibits a higher CO_2 binding affinity than CH_4 and N_2 throughout the adsorption process. **ZJNU-40a** has a slightly lower isosteric heat of CO_2 adsorption than **NOTT-101**, indicating that the binding sites can play even more important roles than the interaction strengths in enhancing carbon dioxide uptake and thus gas separation selectivities.[1c] Such phenomena are even more clearly demonstrated in unique UTSA-16 because of its extraordinarily high carbon dioxide capture and separation.[2c] The introduction of the heterocyclic functional sites and the smaller pore sizes within **ZJNU-40a** have played the most important roles for its better performance than **NOTT-101** for carbon dioxide capture and separation.

In summary, we have synthesized a new NbO-type MOF, **ZJNU-40**, by utilizing a unique tetracarboxylate containing benzothiadiazole as a polarized functional site. With moderately high BET surface area, two types of nanoscopic cages, open metal sites, accessible donor sites, and smaller pore spaces within the framework, the activated **ZJNU-40a** exhibits higher CO_2 uptake capacity as well as better adsorption selectivity of CO_2 over CH_4 and N_2, and thus better CO_2 capture performance than the isoreticular **NOTT-101**. This work demonstrated that incorporation of a polarized heteroaromatic ring into the framework provides a promising route to improve CO_2 gas sorption and selectivity and thus to produce materials with enhanced CO_2 separation performance.

This work was supported by the National Natural Science Foundation of China (No. 21301156), Open Research Fund of Top Key Discipline of Chemistry in Zhejiang Provincial Colleges and Key Laboratory of the Ministry of Education for Advanced Catalysis Materials (ZJHX201313), and Grant AX-1730 from the Welch Foundation (B.C.).

Notes and references

1 (*a*) K. Sumida, D. L. Rogow, J. A. Mason, T. M. McDonald, E. D. Bloch, Z. R. Herm, T.-H. Bae and J. R. Long, *Chem. Rev.*, 2012, **112**, 724–781; (*b*) J.-R. Li, J. Sculley and H.-C. Zhou, *Chem. Rev.*, 2012, **112**, 869–932; (*c*) Z. Zhang, Z.-Z. Yao, S. Xiang and B. Chen, *Energy Environ. Sci.*, 2014, **7**, 2868–2899; (*d*) J.-P. Zhang and X.-M. Chen, *J. Am. Chem. Soc.*, 2009, **131**, 5516–5521; (*e*) R.-J. Li, M. Li, X.-P. Zhou, D. Li and M. O'Keeffe, *Chem. Commun.*, 2014, **50**, 4047–4049; (*f*) Y.-X. Tan, Y.-P. He and J. Zhang, *Chem. Commun.*, 2011, **47**, 10647–10649; (*g*) D.-S. Zhang, Z. Chang, Y.-F. Li, Z.-Y. Jiang, Z.-H. Xuan, Y.-H. Zhang, J.-R. Li, Q. Chen, T.-L. Hu and X.-H. Bu, *Sci. Rep.*, 2013, **3**, 3312; (*h*) Y.-L. Huang, Y.-N. Gong, L. Jiang and T.-B. Lu, *Chem. Commun.*, 2013, **49**, 1753–1755.

2 (*a*) A. R. Millward and O. M. Yaghi, *J. Am. Chem. Soc.*, 2005, **127**, 17998–17999; (*b*) S. R. Caskey, A. G. Wong-Foy and A. J. Matzger, *J. Am. Chem. Soc.*, 2008, **130**, 10870–10871; (*c*) S. Xiang, Y. He, Z. Zhang, H. Wu, W. Zhou, R. Krishna and B. Chen, *Nat. Commun.*, 2012, **3**, 954; (*d*) P. Nugent, Y. Belmabkhout, S. D. Burd, A. J. Cairns, R. Luebke, K. Forrest, T. Pham, S. Ma, B. Space, L. Wojtas, M. Eddaoudi and M. J. Zaworotko, *Nature*, 2013, **495**, 80–84.

3 (*a*) X. Lin, I. Telepeni, A. J. Blake, A. Dailly, C. M. Brown, J. M. Simmons, M. Zoppi, G. S. Walker, K. M. Thomas, T. J. Mays, P. Hubberstey, N. R. Champness and M. Schröder, *J. Am. Chem. Soc.*, 2009, **131**, 2159–2171; (*b*) Y. He, W. Zhou, T. Yildirim and B. Chen, *Energy Environ. Sci.*, 2013, **6**, 2735–2744.

4 (*a*) M. Zhang, Q. Wang, Z. Lu, H. Liu, W. Liu and J. Bai, *CrystEngComm*, 2014, **16**, 6287–6290; (*b*) B. Zheng, H. Liu, Z. Wang, X. Yu, P. Yia and J. Bai, *CrystEngComm*, 2013, **15**, 3517–3520; (*c*) T. K. Prasad, D. H. Hong and M. P. Suh, *Chem. – Eur. J.*, 2010, **16**, 14043–14050; (*d*) Z. Wang, B. Zheng, H. Liu, X. Lin, X. Yu, P. Yi and R. Yun, *Cryst. Growth Des.*, 2013, **13**, 5001–5006; (*e*) N. H. Alsmail, M. Suyetin, Y. Yan, R. Cabot, C. P. Krap, J. Lü, T. L. Easun, E. Bichoutskaia, W. Lewis, A. J. Blake and M. Schröder, *Chem. – Eur. J.*, 2014, **20**, 7317–7324.

5 (*a*) M. Li, D. Li, M. O'Keeffe and O. M. Yaghi, *Chem. Rev.*, 2014, **114**, 1343–1370; (*b*) R.-J. Li, M. Li, X.-P. Zhou, S. W. Ng, M. O'Keeffe and D. Li, *CrystEngComm*, 2014, **16**, 6291–6295.

6 D. Sun, S. Ma, J. M. Simmons, J.-R. Li, D. Yuan and H.-C. Zhou, *Chem. Commun.*, 2010, **46**, 1329–1331.

7 R. D. Kennedy, V. Krungleviciute, D. J. Clingerman, J. E. Mondloch, Y. Peng, C. E. Wilmer, A. A. Sarjeant, R. Q. Snurr, J. T. Hupp,

T. Yildirim, O. K. Farha and C. A. Mirkin, *Chem. Mater.*, 2013, **25**, 3539–3543.
8 H.-M. Wen, B. Li, D. Yuan, H. Wang, T. Yildirim, W. Zhou and B. Chen, *J. Mater. Chem. A*, 2014, **2**, 11516–11522.
9 Z. Wang, B. Zheng, H. Liu, P. Yi, X. Li, X. Yu and R. Yun, *Dalton Trans.*, 2013, **42**, 11304–11311.
10 Y. He, S. Xiang, Z. Zhang, S. Xiong, C. Wu, W. Zhou, T. Yildirim, R. Krishna and B. Chen, *J. Mater. Chem. A*, 2013, **1**, 2543–2551.
11 Z. Liang, J. Du, L. Sun, J. Xu, Y. Mu, Y. Li, J. Yu and R. Xu, *Inorg. Chem.*, 2013, **52**, 10720–10722.
12 R. Krishna and J. R. Long, *J. Phys. Chem. C*, 2011, **115**, 12941–12950.

Published on 20 August 2014. Downloaded by Universiteit van Amsterdam on 17/09/2014 07:49:39.

 This journal is © The Royal Society of Chemistry 2014

Electronic Supplementary Material (ESI) for ChemComm.
This journal is © The Royal Society of Chemistry 2014

Supporting Information for the manuscript

Enhanced CO_2 Sorption and Selectivity by Functionalization of a NbO-type Metal-Organic Framework with Polarized Benzothiadiazole Moieties

Chengling Song,[a] Yabing He,[a*] Bin Li,[b] Yajing Ling,[a] Hailong Wang,[b] Yunlong Feng,[a] Rajamani Krishna,[c] Banglin Chen[b*]

[a] College of Chemistry and Life Sciences, Zhejiang Normal University, Jinhua 321004, China. E-mail: heyabing@zjnu.cn.

[b] Department of Chemistry, University of Texas at San Antonio, One UTSA Circle, San Antonio, Texas 78249-0698, USA. E-mail: banglin.chen@utsa.edu; Fax: +1-210-458-7428

[c] Van't Hoff Institute for Molecular Sciences, University of Amsterdam Science Park 904, 1098 XH Amsterdam (The Netherlands)

General remarks

All starting materials and reagents for synthesis were commercially available and used as received. The ^{1}H NMR and ^{13}C NMR spectra were recorded on a Bruke Avance 600 spectrometer. Fourier transform infrared (FTIR) spectrum was recorded using a Nicolet 5DX FT-IR spectrometer. Thermogravimetric analyses (TGA) were carried out using a Netzsch STA 449C thermal analyzer with a heating rate of 5 ^{o}C min^{-1} in a flowing nitrogen atmosphere (10 mL min^{-1}). Powder X-ray diffraction (PXRD) patterns were recorded on a Philips PW3040/60 automated powder diffractometer, using Cu-K$_\alpha$ radiation (λ = 1.542 Å) with a 2θ range of 5–45°. The elemental analyses were performed with Perkin–Elmer 240 CHN analyzers. The crystal data were collected on a Bruker APEX II diffractometer equipped with a graphite-monochromatized Mo-K$_\alpha$ radiation (λ = 0.71073 Å) at 296(2) K. Data intensity was corrected by Lorentz-polarization factors and empirical absorption. The structures were solved by direct methods and expanded with difference Fourier techniques. All calculations were performed using SHELXS-97 and SHELXL-97 program packages. A Micromeritics ASAP 2020 surface area analyzer was used to measure gas adsorption isotherms. To have a guest-free framework, the fresh sample was guest-exchanged with dry acetone at least 10 times, filtered and vacuumed at 373 K until the outgas rate was 6 μmHg min^{-1} prior to measurements. A sample of 113.7 mg was used for the sorption measurements and was maintained at 77 K with liquid nitrogen, and at 273 K with an ice–water bath. As the center-controlled air conditioner was set up at 23 ^{o}C, a water bath was used for adsorption isotherms at 296 K.

Synthesis and characterization of the organic building block (H_4L)

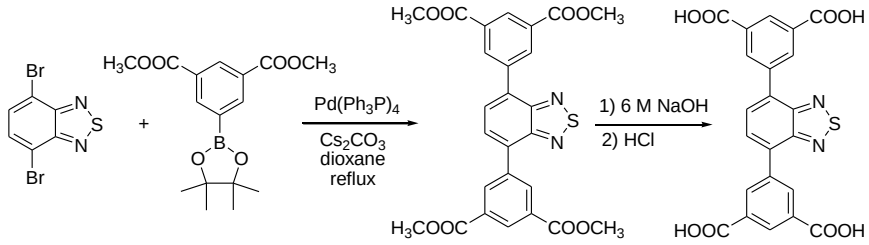

Scheme 1 Synthetic route to the organic linker used to construct **ZJNU-40**.

To a mixture of 4,7-dibromobenzo[c][1,2,5]thiadiazole (0.50 g, 1.70 mmol), dimethyl 5-(pinacolboryl)isophthalate (1.20 g, 3.74 mmol), Cs_2CO_3 (1.66 g, 5.10 mmol) and $Pd(PPh_3)_4$ (0.10 g, 0.09 mmol) were added dry dioxane (40 mL). The resulting mixture was stirred under reflux under a nitrogen atmosphere for 72 hr. After removal of the solvents, CH_2Cl_2 (100 mL) and H_2O (100 mL) were added. The mixture was filtered, washed with water and CH_2Cl_2 sequentially, and dried under vacuum. The solid was hydrolyzed with 6 M NaOH, filtered and acidified with concentrated HCl to afford the target compound as a yellow solid in 66% yield (0.52 g, 1.12 mmol). ^{1}H NMR (DMSO-d_6, 600.1 MHz) δ (ppm): 13.50 (s, br, 4H), 8.81 (d, J = 1.8 Hz, 4H), 8.57 (t, J = 1.8 Hz, 2H), 8.15 (s, 2H); ^{13}C NMR (DMSO-d_6, 150.9 MHz) δ (ppm): 166.41, 152.95, 137.32, 133.66, 131.67, 130.97, 129.63, 128.89; selected FTIR (KBr, cm^{-1}): 1732, 1709, 1601, 1554, 1441, 1404, 1304, 1271, 1215, 1161, 1124, 916, 895, 854, 802, 756, 708, 685, 667, 548, 519.

Synthesis and characterization of ZJNU-40

A mixture of the organic linker H_4L (5.0 mg, 10.7 μmol) and $Cu(NO_3)_2{\cdot}3H_2O$ (15.0 mg, 62.1 μmol) was dissolved into a mixed solvent of *N*,*N*-diethylformamide (DEF) and H_2O (1.5 mL / 0.08 mL) in a screw-capped vial (20 mL). 50 μL of 6 M HCl were then added. The vial was capped and heated at 353 K for 96 h. Blue rhombic crystals were obtained in 67% yield. **ZJNU-40** can be best formulated as $[Cu_2L(H_2O)_2]{\cdot}4DEF{\cdot}6H_2O$ on the basis of single-crystal X-ray diffraction structure determination, TGA and microanalysis. Selected FTIR (KBr, cm^{-1}): 1660, 1591, 1568, 1495, 1444, 1417, 1381, 1093, 1049, 879, 777, 754, 729; TGA data for loss of $4DEF+8H_2O$, calcd: 46.6%, found: 48.0%; anal. for $C_{42}H_{64}Cu_2N_6O_{18}S$, calcd: C, 45.85%, H, 5.86%, N, 7.64%; found: C, 48.59%, H, 5.90%, N, 7.55%.

Fitting of pure-component isotherms

The measured experimental data on *excess* loadings, q^{excess}, of the pure components CO_2, CH_4, and N_2 in **ZJNU-40a** and **NOTT-101**, were first converted to absolute loadings, q, using

$$q = q^{excess} + \frac{pV_{pore}}{ZRT} \quad (1)$$

where Z is the compressibility factor. The Peng-Robinson equation of state was used to estimate Z. The accessible pore volume for **ZJNU-40a** and **NOTT-101** are 0.8806 $cm^3\ g^{-1}$ and 1.0485 $cm^3\ g^{-1}$, respectively.

The absolute component loadings were fitted with the Langmuir model

$$q = q_{sat}\frac{bp}{1+bp} \quad (2)$$

with T-dependent parameter b

$$b = b_0 \exp\left(\frac{E}{RT}\right) \quad (3)$$

The Langmuir parameters for adsorption of CO_2 are provided in *Tables S3*, and *S4* for **ZJNU-40a** and **NOTT-101**.

Figure S6 provides a comparison of the experimental isotherm data for (a) CO_2, (b) CH_4, and (c) N_2 in **ZJNU-40a** with the isotherm fits. *Figure S7* provides a comparison of the experimental isotherm data for (a) CO_2, (b) CH_4, and (c) N_2 in **NOTT-101** with the isotherm fits. For all guest/host combinations, the isotherm fits are excellent.

Isosteric heat of adsorption

The isosteric heat of adsorption, Q_{st}, defined as

$$Q_{st} = RT^2\left(\frac{\partial \ln p}{\partial T}\right)_q \quad (4)$$

was determined using the Clausius-Clapeyron equation by fitting the adsorption isotherms taken at 273 and 296 K to a Langmuir expression. The values of Q_{st} for CO_2, CH_4, and N_2 in **ZJNU-40a**, and **NOTT-101** are shown in *Figure S17*.

IAST calculations of adsorption selectivities and uptake capacities

The selectivity of preferential adsorption of component *1* over component *2* in a mixture containing *1* and *2*, perhaps in the presence of other components too, can be formally defined as

$$S_{ads} = \frac{q_1/q_2}{p_1/p_2} \quad (5)$$

In equation (5), q_1 and q_2 are the absolute component loadings of the adsorbed phase in the mixture. These component loadings are also termed the uptake capacities. We calculate the values of q_1 and q_2 using the Ideal Adsorbed Solution Theory (IAST) of Myers and Prausnitz.[1]

Figures S8a and *S8b* present the values of the adsorption selectivity for (a) 50/50

CO_2/CH_4, and (b) 5/95 CO_2/CH_4 gas mixtures maintained at isothermal conditions at 296 K in **ZJNU-40a**, and **NOTT-101**. We note that **ZJNU-40a** has higher selectivity towards CO_2 for both mixture compositions.

ZJNU-40a has a higher selectivity towards CO_2 for adsorption from 15/85 CO_2/N_2 gas mixtures; see *Figure S8c*.

Besides the adsorption selectivities, the separation performance is also dictated by uptake capacities. *Figures S9a, S9b,* and *S9c* present IAST calculations for uptake of CO_2 from (a) 50/50 CO_2/CH_4, (b) 5/95 CO_2/CH_4, and (c) 15/85 CO_2/N_2 gas mixtures maintained at isothermal conditions at 296 K in **ZJNU-40a**, and **NOTT-101**. **ZJNU-40a** has higher uptake of CO_2 in all three cases.

The combination of higher selectivity and higher uptake of CO_2 is most desirable and leads to enhanced sepatations in fixed beds.

Transient breakthroughs in fixed bed adsorbers

The performance of industrial fixed bed adsorbers is dictated by a combination of *adsorption selectivity* and *uptake capacity*. For a proper comparison of various MOFs, we perform transient breakthrough simulations using the simulation methodology described in the literature.[2-6] For the breakthrough simulations, the following parameter values were used: length of packed bed, L = 0.3 m; voidage of packed bed, ε = 0.4; superficial gas velocity at inlet, u = 0.04 m s^{-1}; see schematic in *Figure S10*.

The transient breakthrough simulation results are presented in terms of a dimensionless time, τ, defined by dividing the actual time, t, by the characteristic time, $\frac{L\varepsilon}{u}$.

Figure S11 compares 50/50 CO_2/CH_4 mixture breakthrough characteristics as a function of the dimensionless time in an adsorber packed with **ZJNU-40a** and **NOTT-101**. For both materials the sequence of breakthroughs is CH_4, and CO_2 that is dictated by the adsorption strengths; the more strongly adsorbing CO_2 elutes last in the sequence. The breakthrough of CO_2 occurs at a later time with **ZJNU-40a** and this material has the better separation performance. The reason for the improved separation can be traced to two separate factors: (a) higher CO_2 uptake capacity of **ZJNU-40a**, and (b) higher CO_2/CH_4 adsorption selectivities.

In natural gas purification processes, the primary objective is to produce CH_4 with a specified purity level, which is typically 500 ppm CO_2, *i.e.* 0.05 mole % CO_2. Let us compare the productivities of pure CH_4 that fulfills the specified impurity level for CO_2. *Figure S12* presents a comparison of the % CH_4 exiting the adsorber packed with **ZJNU-40a**, and **NOTT-101**. During the time interval $\Delta\tau$, 99.95%+ pure CH_4 can be produced. These amounts can be determined from a material balance on the fixed bed adsober; the productivities are 2.84 mol *per* kg of **ZJNU-40a**, and 1.78 mol *per* kg of **NOTT-101**. This implies that **ZJNU-40a** has a 50% higher productivity than **NOTT-101**.

Let us consider separations of 5/95 CO_2/CH_4 mixtures. *Figure S13* compares 5/95 CO_2/CH_4 mixture breakthrough characteristics of **ZJNU-40a** and **NOTT-101**. *Figure*

S14 presents a comparison of the % CH_4 exiting the adsorber packed with **ZJNU-40a**, and **NOTT-101**. From a material balance on the fixed bed adsober; the productivities are 5.80 mol *per* kg of **ZJNU-40a**, and 3.62 mol *per* kg of **NOTT-101**. These productivity values are higher than the corresponding ones for 50/50 mixtures because of the lower amount of CO_2 that needs to be captured. For 5/95 CO_2/CH_4 mixtures, **ZJNU-40a** has a 60% higher productivity than **NOTT-101**.

Let us now compare separations of 15/85 CO_2/N_2 gas mixtures that is relevant for CO_2 capture from flue gases. *Figure S15* presents the 15/85 CO_2/N_2 mixture breakthrough characteristics as a function of the dimensionless time in an adsorber packed with **ZJNU-40a**, and **NOTT-101** at a total pressure of 100 kPa. N_2 with a purity of 99.95% can be produced during the time interval $\Delta\tau$, as indicated in *Figure S16*. The productivity can be determined to be 3.29 mol *per* kg of **ZJNU-40a**, and 2.08 mol *per* kg of **NOTT-101**.

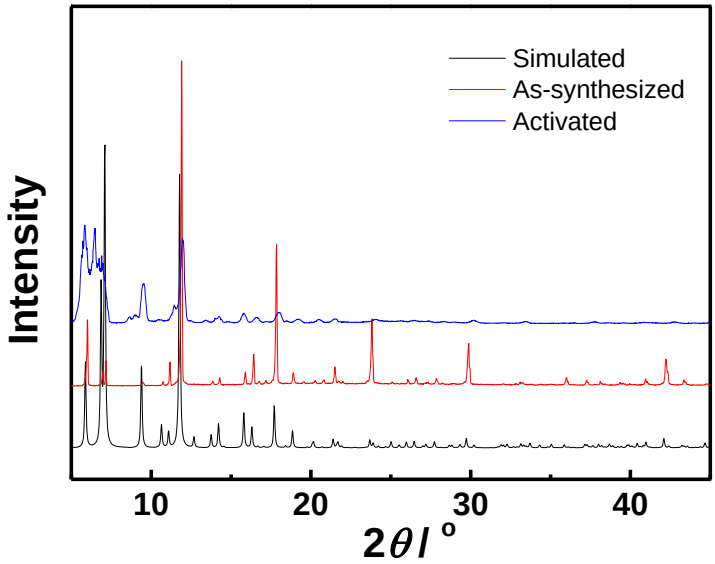

Fig. S1 PXRD patterns of the as-synthesized **ZJNU-40** (red) and the activated **ZJNU-40a** (blue), along with the one simulated from the cif file (black).

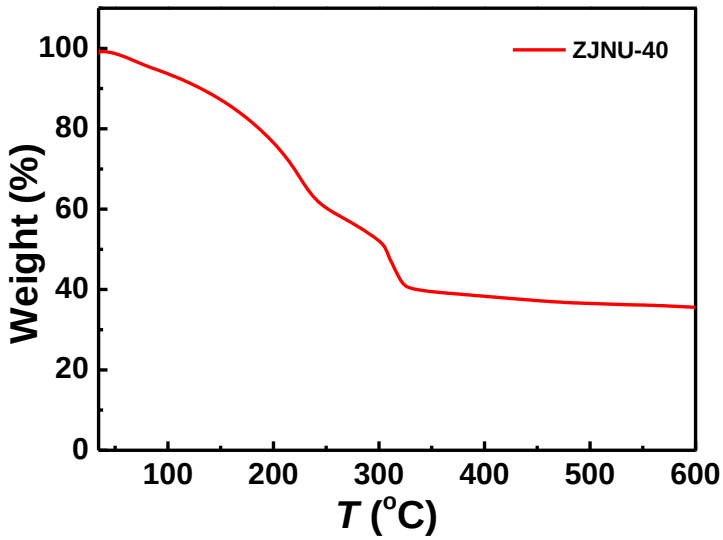

Fig. S2 TGA curve of the as-synthesized **ZJNU-40** under a nitrogen atmosphere.

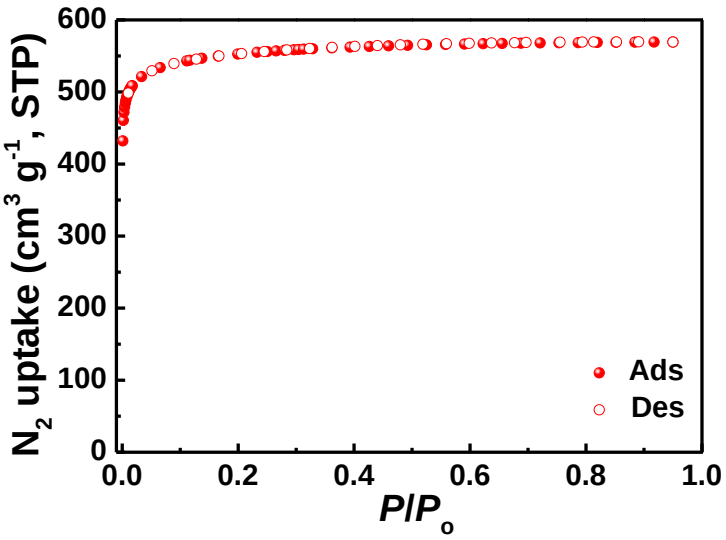

Fig. S3 N_2 sorption isotherm of **ZJNU-40a** at 77 K. The solid and open symbols represent adsorption and desorption, respectively.

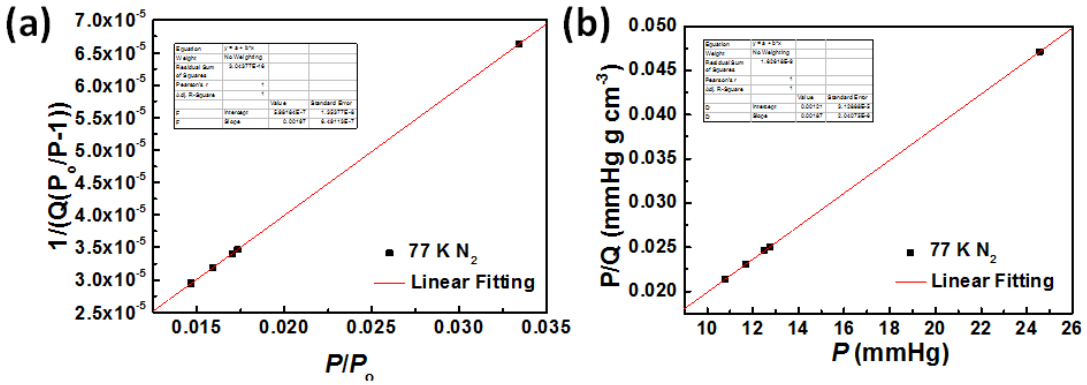

Fig. S4 BET and Langmuir analysis from N_2 adsorption isotherm at 77 K.

S_{BET} = 1/(0.00197 + 5.98184×10^{-7})/22414 ×6.023 ×10^{23} ×0.162 ×10^{-18} = 2209 m^2 g^{-1}

$S_{Langmuir}$ = (1/0.00187)/22414 ×6.023 ×10^{23} ×0.162 ×10^{-18} = 2328 m^2 g^{-1}

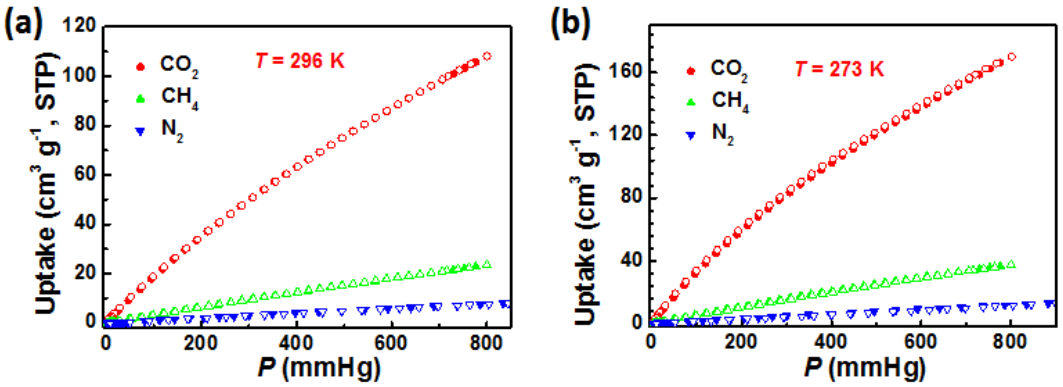

Fig. S5 CO_2, CH_4 and N_2 sorption isotherms of **ZJNU-40a** at 296 K (a), and 273 K (b). The solid and open symbols represent adsorption and desorption, respectively.

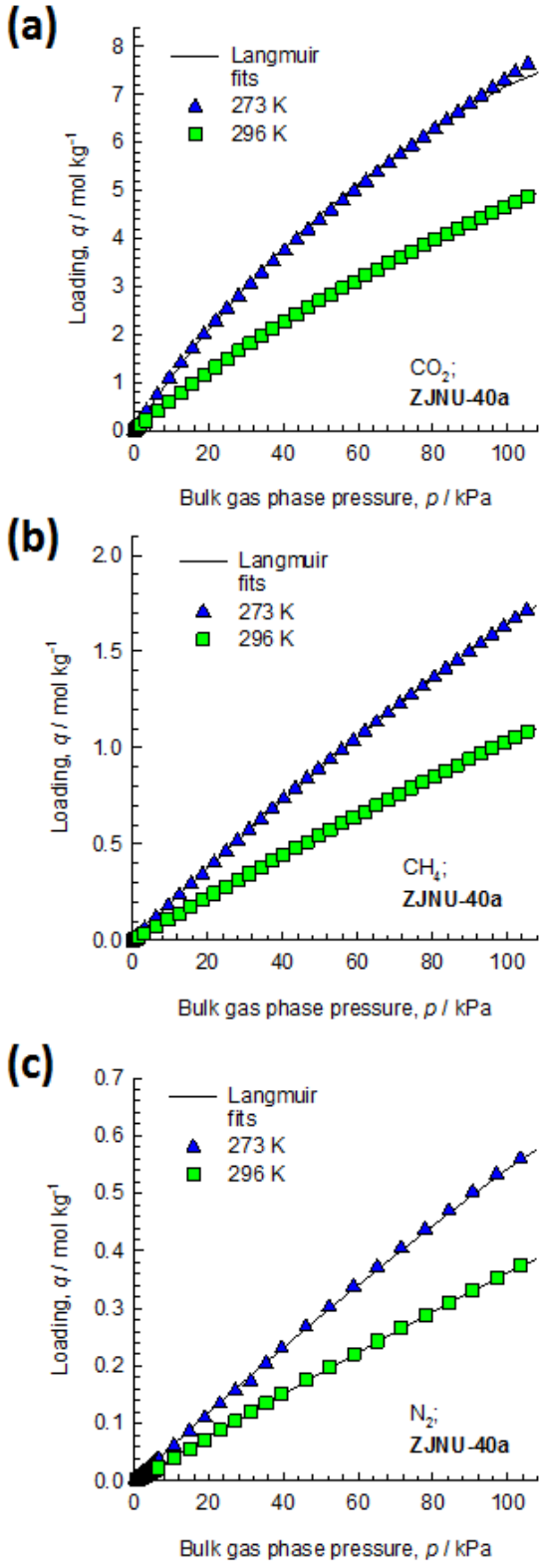

Fig. S6 Comparison of the pure-component isotherm data for (a) CO_2, (b) CH_4, and (c) N_2 in **ZJNU-40a** with the fitted isotherms (shown by continuous solid lines) at 273 K, and 296 K.

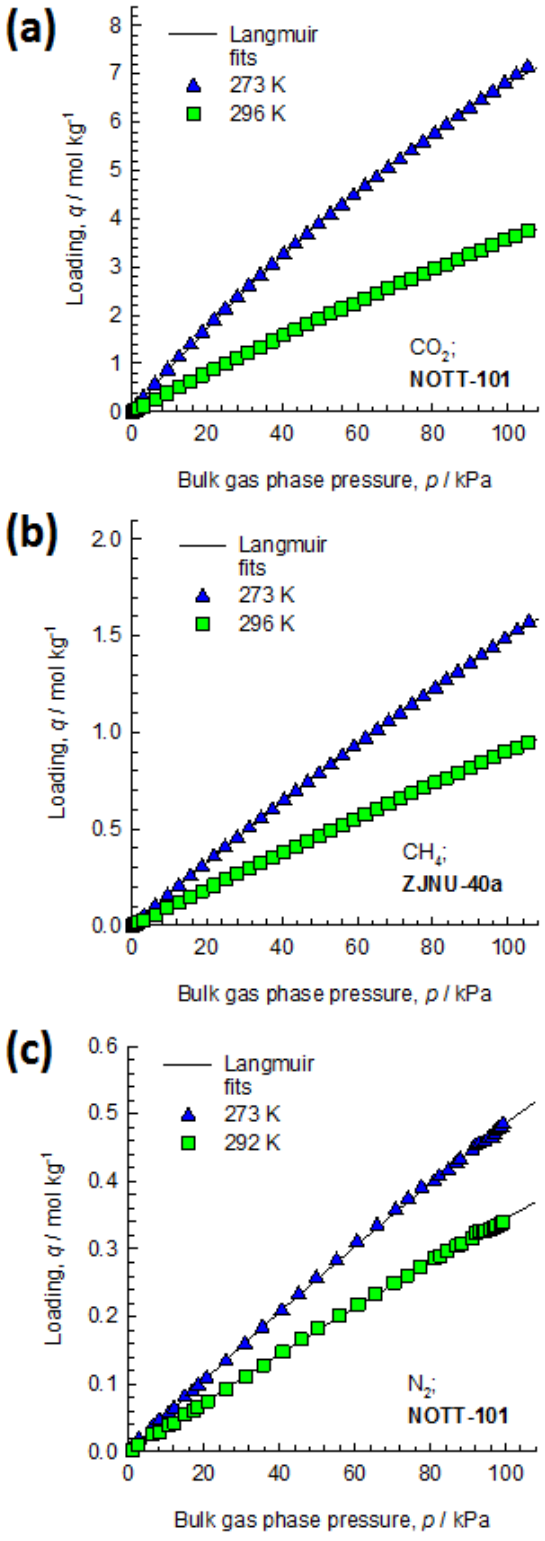

Fig. S7 Comparison of the pure-component isotherm data for (a) CO_2, (b) CH_4, and (c) N_2 in **NOTT-101** with the fitted isotherms (shown by continuous solid lines).

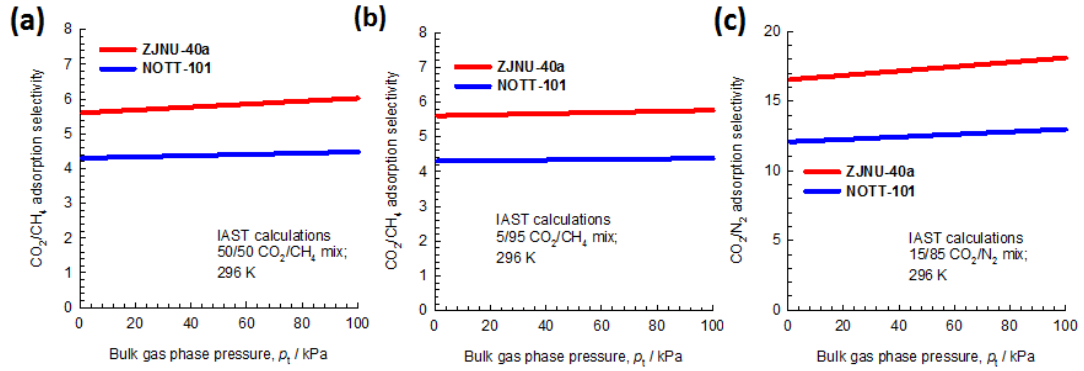

Fig. S8 Calculations using Ideal Adsorbed Solution Theory (IAST) of Myers and Prausnitz[1] for adsorption selectivitites for (a) 50/50 CO_2/CH_4, (b) 5/95 CO_2/CH_4, and (c) 15/85 CO_2/N_2 gas mixtures maintained at isothermal conditions at 296 K in **ZJNU-40a**, and **NOTT-101**.

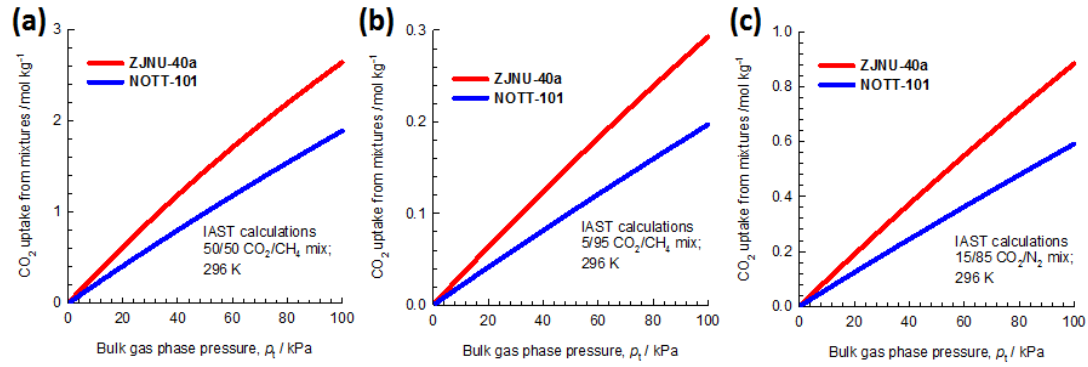

Fig. S9 Calculations using Ideal Adsorbed Solution Theory (IAST) of Myers and Prausnitz[1] for uptake of CO_2 from (a) 50/50 CO_2/CH_4, (b) 5/95 CO_2/CH_4, and (c) 15/85 CO_2/N_2 gas mixtures maintained at isothermal conditions at 296 K in **ZJNU-40a**, and **NOTT-101**.

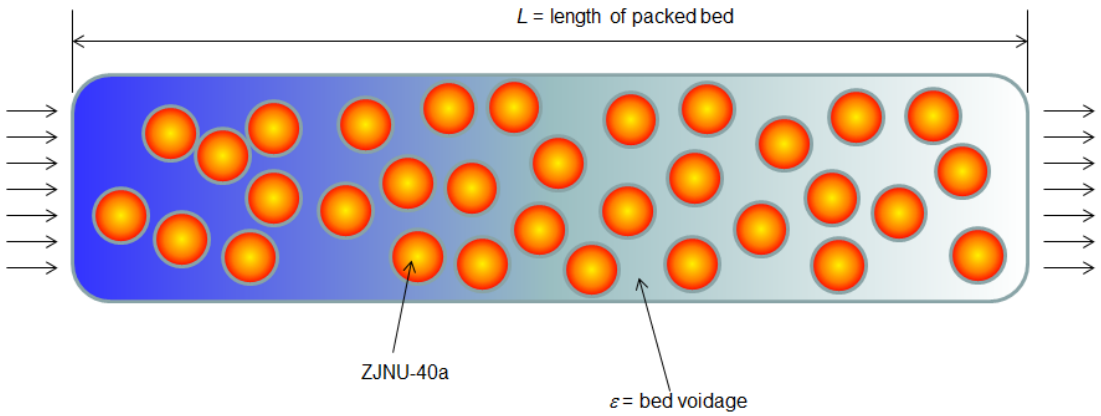

Fig. S10 Schematic of the breakthrough apparatus. The tube length L = 0.3 m. The apparatus is operated at 296 K, and at a total gas pressure of 200 kPa or 100 kPa. The bed porosity, ε = 0.4. The interstitial gas velocity, v = 0.04 m s^{-1}.

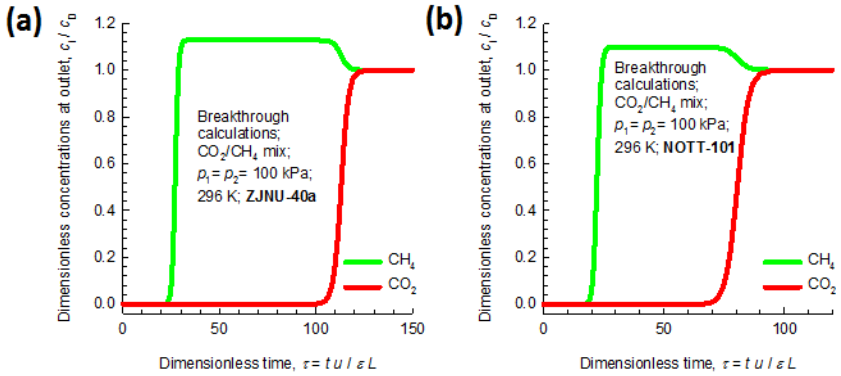

Fig. S11 50/50 CO_2/CH_4 mixture breakthrough characteristics as a function of the dimensionless time in an adsorber packed with (a) **ZJNU-40a**, and (b) **NOTT-101** and maintained at isothermal conditions at 296 K. In these calculations, the total pressure is maintained at 200 kPa.

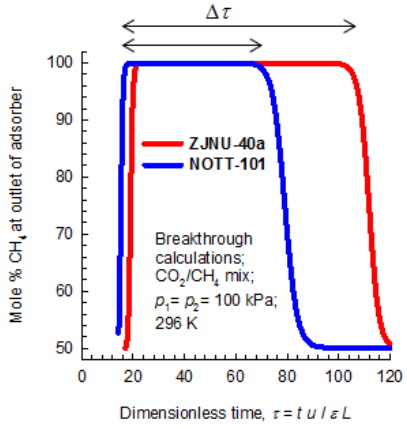

Fig. S12 Comparison of the %CH_4 exiting the adsorber packed with **ZJNU-40a**, and **NOTT-101** fed with 50/50 CO_2/CH_4 gas mixtures at 200 kPa total pressure and 296 K.

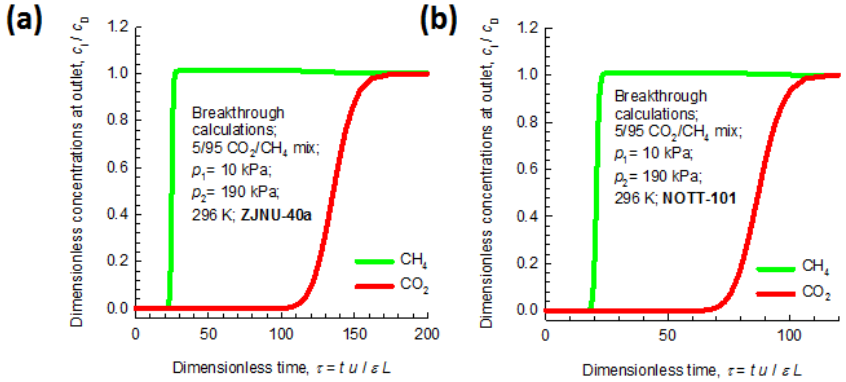

Fig. S13 5/95 CO_2/CH_4 mixture breakthrough characteristics as a function of the dimensionless time in an adsorber packed with (a) **ZJNU-40a**, and (b) **NOTT-101** and maintained at isothermal conditions at 296 K. In these calculations, the total pressure is maintained at 200 kPa.

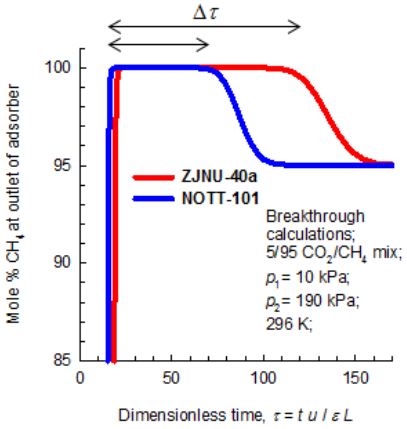

Fig. S14 Comparison of the %CH_4 exiting the adsorber packed with **ZJNU-40a**, and **NOTT-101** fed with 5/95 CO_2/CH_4 gas mixtures at 200 kPa total pressure and 296 K.

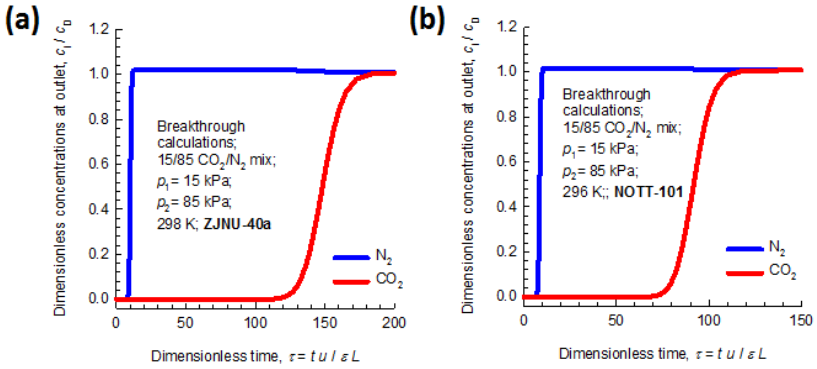

Fig. S15 15/85 CO_2/N_2 mixture breakthrough characteristics as a function of the dimensionless time in an adsorber packed with (a) **ZJNU-40a**, and (b) **NOTT-101** and maintained at isothermal conditions at 296 K. In these calculations, the total pressure is maintained at 100 kPa.

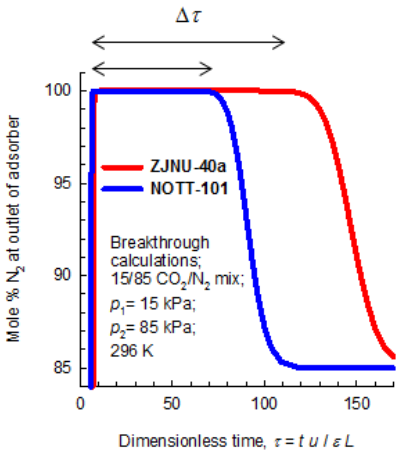

Fig. S16 Comparison of the % N_2 exiting the adsorber packed with **ZJNU-40a**, and **NOTT-101** fed with 15/85 CO_2/N_2 gas mixtures at 100 kPa total pressure and 296 K.

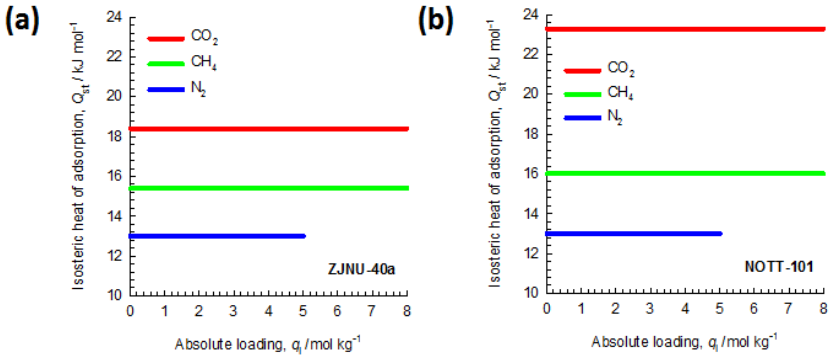

Fig. S17 Isosteric heats of adsorption of CO_2, CH_4, and N_2 in **ZJNU-40a** (a) and **NOTT-101** (b).

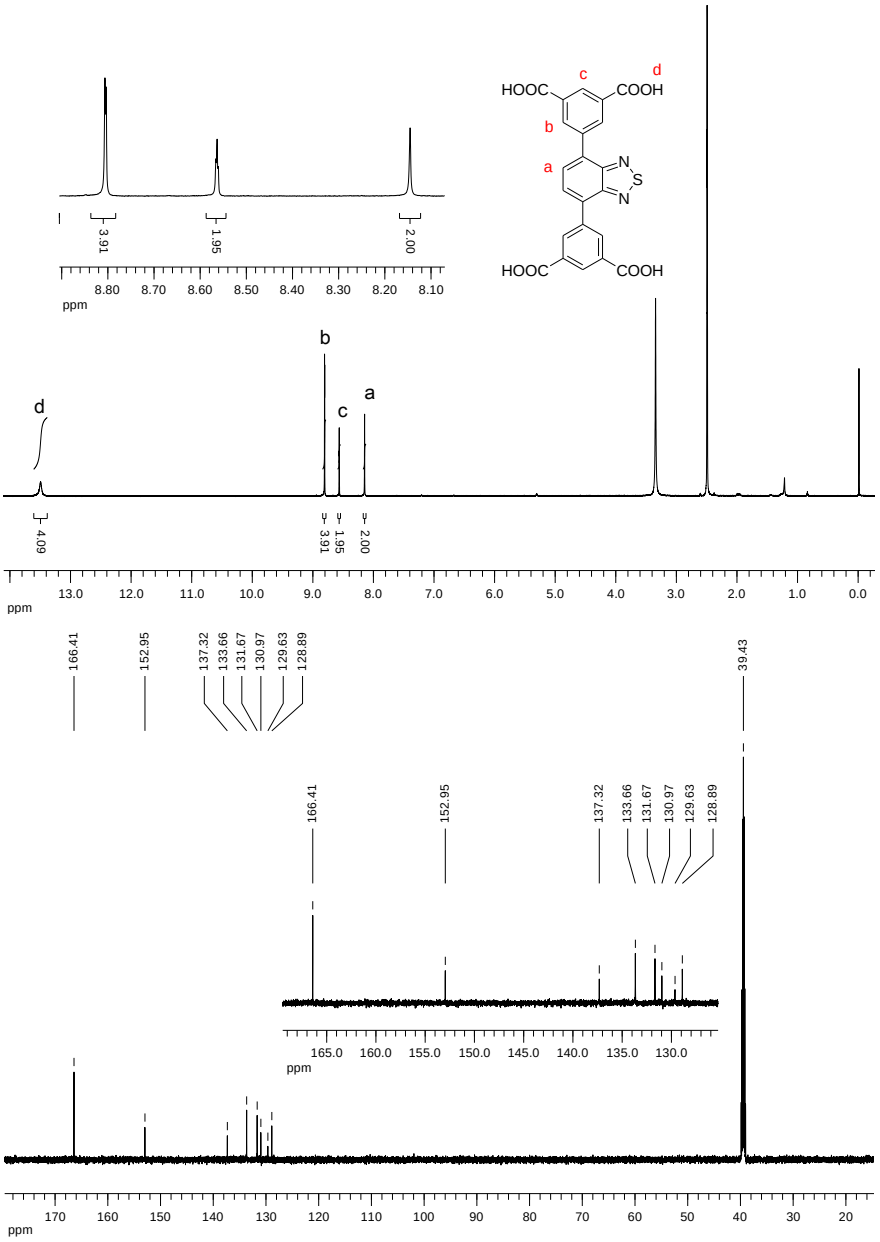

Fig. S18 ^{1}H NMR (DMSO-d_6, 600.1 MHz) and ^{13}C NMR (DMSO-d_6, 150.9 MHz) spectra of the organic linker H_4L.

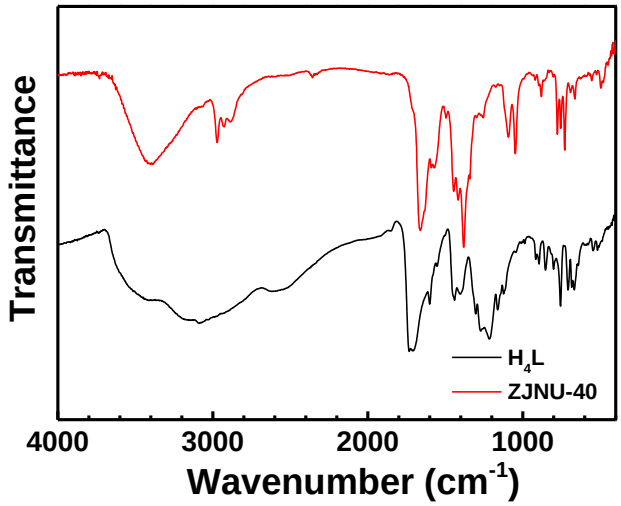

Fig. S19 FTIR spectra of the organic linker H_4L (black) and as-synthesized **ZJNU-40** (red).

Table S1. Crystal data and structure refinement for **ZJNU-40**.

Empirical formula	$C_{66}H_{24}Cu_6N_6O_{32}S_3$
Formula weight	1890.42
Temperature (K)	296(2)
Wavelength (Å)	0.71073
Crystal system, space group	Trigonal, *R*-3m
Unit cell dimensions	a = 18.819(4) Å b = 18.819(4) Å c = 38.603(15) Å $\alpha = 90^o$ $\beta = 90^o$ $\gamma = 120^o$
Volume (Å^3)	11840(6)
Z, Calculated density (g cm^{-3})	3, 0.795
Absorption coefficient (mm^{-1})	0.877
F(000)	2820
Crystal size (mm)	0.2 × 0.18 × 0.12
θ range for data collection (^{o})	3.27 to 27.56
Limiting indices	$-24 \le h \le 24$ $-24 \le k \le 24$ $-50 \le l \le 50$
Reflections collected / unique	42313 / 3293 (R_{int} = 0.0339)
Completeness to θ = 27.56	99.0%
Absorption correction	Semi-empirical from equivalents
Max. and min. transmission	0.900 and 0.839
Refinement method	Full-matrix least-squares on F^2
Data / restraints / parameters	3293 / 1 / 124
Goodness-of-fit on F^2	1.132
Final R indices [$I > 2\sigma(I)$]	R_1 = 0.0544, wR_2 = 0.1823
R indices (all data)	R_1 = 0.0612, wR_2 = 0.1910
Largest diff. peak and hole (e.Å^{-3})	1.137 and -0.335
CCDC	1014276

Table S2. BET surface area, pore volume and CO_2 adsorption of the reported Cu-based NbO-type MOFs.

MOFs	BET[a] ($m^2\ g^{-1}$)	V_p[b] ($cm^3\ g^{-1}$)	CO_2 uptake under 1 atm at RT ($cm^3\ g^{-1}$)	Q_{st}[c] (kJ mol^{-1})	Selectivity[d] CO_2/CH_4	Selectivity[d] CO_2/N_2	*Ref.*
ZJNU-40	**2209**	**0.8806**	**108**	**18.4**	**6.6**	**22.9**	**This work**
HNUST-1	1400	0.571	93	31.2			[7]
MOF-505	1547		73				[8]
UTSA-40	1630	0.65	73	24.0	5.6		[9]
Cu_2dbip	1773	0.81	122	28.1		21.1	[10]
Cu_2ebtc	1852	1.008					[11]
ZJU-25	2124	1.183	83		5.5		[12]
SNU-50	2300	1.08	80	25.8			[13]
HNUST-2	2366	0.97		23.5	4.9	22.9	[14]
NJU-Bai14	2384		100	24.5			[15]
HNUST-3	2421	0.99	84.5	24.8	7.9	26.1	[16]
NOTT-125a	2447	1.1	93		4.8	16	[17]
NU-135	2530	1.02	79	25.5	4	14.5	[18]
NOTT-101	2805	1.080	83	23.3	4.6		[3]
ZJU-5	2823	1.074	85				[19]
Cu_2abtc	(2850)[e]	1.00					[20]
NJU-Bai12	3038	1.135		23.5	5.0	24.6	[21]
NOTT-102	3342	1.268	72[f]		4.84		[3]

[a] BET surface area; [b] pore volume; [c] the initial heat of CO_2 adsorption; [d] Henry's Law selectivity at room temperature, [e] Langmuir surface area, [f] the data measured at this work.

Table S3 Langmuir parameters for adsorption of CO_2, CH_4, and N_2 in **ZJNU-40a**.

	q_{sat} (mol kg^{-1})	b_0 (Pa^{-1})	E (kJ mol^{-1})
CO_2	17.8	2.05×10^{-9}	18.4
CH_4	10.3	2.14×10^{-9}	15.4
N_2	5	3.96×10^{-9}	13

Table S4. Langmuir parameters for adsorption of CO_2, CH_4, and N_2 in **NOTT-101**. The pure-component isotherm data for CO_2, CH_4, are from data measured in this work at temperatures of 273 K and 296 K. The pure-component isotherm data for N_2 are from Perry et al;[22] their data are reported at 273 K and 292 K.

	q_{sat} (mol kg^{-1})	b_0 (Pa^{-1})	E (kJ mol^{-1})
CO_2	26	1.24×10^{-10}	23.3
CH_4	14	1.04×10^{-9}	16
N_2	5	3.51×10^{-9}	13

Notation

b	Langmuir constant for species i at adsorption site A, Pa^{-1}
c_i	molar concentration of species i in gas mixture, mol m^{-3}
c_{i0}	molar concentration of species i in gas mixture at inlet to adsorber, mol m^{-3}
E	energy parameter, J mol^{-1}
L	length of packed bed adsorber, m
p_i	partial pressure of species i in mixture, Pa
p_t	total system pressure, Pa
q_i	component molar loading of species i, mol kg^{-1}
Q_{st}	isosteric heat of adsorption, J mol^{-1}
t	time, s
T	absolute temperature, K
u	superficial gas velocity in packed bed, m s^{-1}

Greek letters

ε	voidage of packed bed, dimensionless
τ	time, dimensionless

Reference

1. A. L. Myers and J. M. Prausnitz, *A.I.Ch.E.J.*, 1965, **11**, 121-127.
2. R. Krishna and J. R. Long, *J. Phys. Chem. C*, 2011, **115**, 12941-12950.
3. Y. He, R. Krishna and B. Chen, *Energy Environ. Sci.*, 2012, **5**, 9107-9120
4. E. D. Bloch, W. L. Queen, R. Krishna, J. M. Zadrozny, C. M. Brown and J. R. Long, *Science*, 2012, **335**, 1606-1610.
5. H. Wu, K. Yao, Y. Zhu, B. Li, Z. Shi, R. Krishna and J. Li, *J. Phys. Chem. C*, 2012, **116**, 16609-16618.
6. D.-L. Chen, H. Shang, W. Zhu and R. Krishna, *Chem. Eng. Sci.*, 2014, **117**, 407-415.
7. B. Zheng, H. Liu, Z. Wang, X. Yu, P. Yia and J. Bai, *CrystEngComm*, 2013, **15**, 3517-3520.
8. A. R. Millward and O. M. Yaghi, *J. Am. Chem. Soc.*, 2005, **127**, 17998-17999.
9. Y. He, S. Xiang, Z. Zhang, S. Xiong, C. Wu, W. Zhou, T. Yildirim, R. Krishna and B. Chen, *J. Mater. Chem. A*, 2013, **1**, 2543-2551.
10. Z. Liang, J. Du, L. Sun, J. Xu, Y. Mu, Y. Li, J. Yu and R. Xu, *Inorg. Chem.*, 2013, **52**, 10720-10722.
11. Y. Hu, S. Xiang, W. Zhang, Z. Zhang, L. Wang, J. Bai and B. Chen, *Chem. Commun.*, 2009, 7551-7553.
12. X. Duan, J. Yu, J. Cai, Y. He, C. Wu, W. Zhou, T. Yildirim, Z. Zhang, S. Xiang, M. O'Keeffe, B. Chen and G. Qian, *Chem. Commun.*, 2013, **49**, 2043-2045.
13. T. K. Prasad, D. H. Hong and M. P. Suh, *Chem. Eur. J.*, 2010, **16**, 14043-14050.
14. Z. Wang, B. Zheng, H. Liu, P. Yi, X. Li, X. Yu and R. Yun, *Dalton Trans.*, 2013, **42**, 11304-11311.
15. M. Zhang, Q. Wang, Z. Lu, H. Liu, W. Liu and J. Bai, *CrystEngComm*, 2014, **16**, 6287-6290.
16. Z. Wang, B. Zheng, H. Liu, X. Lin, X. Yu, P. Yi and R. Yun, *Cryst. Growth Des.*, 2013, **13**, 5001-5006.
17. N. H. Alsmail, M. Suyetin, Y. Yan, R. Cabot, C. P. Krap, J. Lü, T. L. Easun, E. Bichoutskaia, W. Lewis, A. J. Blake and M. Schröder, *Chem. Eur. J.*, 2014, **20**, 7317-7324.
18. R. D. Kennedy, V. Krungleviciute, D. J. Clingerman, J. E. Mondloch, Y. Peng, C. E. Wilmer, A. A. Sarjeant, R. Q. Snurr, J. T. Hupp, T. Yildirim, O. K. Farha and C. A. Mirkin, *Chem. Mater.*, 2013, **25**, 3539-3543.
19. X. Rao, J. Cai, J. Yu, Y. He, C. Wu, W. Zhou, T. Yildirim, B. Chen and G. Qian, *Chem. Commun.*, 2013, **49**, 6719-6721.
20. Y.-G. Lee, H. R. Moon, Y. E. Cheon and M. P. Suh, *Angew. Chem. Int. Ed.*, 2008, **47**, 7741-7745.
21. B. Zheng, R. Yun, J. Bai, Z. Lu, L. Du and Y. Li, *Inorg. Chem.*, 2013, **52**, 2823-2829.
22. J. J. P. IV, S. L. Teich-McGoldrick, S. T. Meek, J. A. Greathouse, M. Haranczyk and M. D. Allendorf, *J. Phys. Chem. C*, 2014, **118**, 11685-11698.